JGR Oceans

RESEARCH ARTICLE
10.1029/2024JC021836

Dynamics and Temporal Variability of the North Atlantic Current in the Iceland Basin (2014–2022)

Tiago S. Dotto[1], N. Penny Holliday[1], Neil Fraser[2], Ben Moat[1], Yvonne Firing[1], Kristin Burmeister[2], Darren Rayner[1], Stuart Cunningham[2], Emma Worthington[3], and William E. Johns[3]

[1]National Oceanography Centre, Southampton, UK, [2]The Scottish Association for Marine Science, Oban, UK, [3]Rosenstiel School of Marine and Atmospheric Science, University of Miami, Miami, FL, USA

Key Points:

- The North Atlantic Current (NAC) volume transport variability was strong at 16–120-day periods associated with the mesoscale activity in the Iceland Basin
- High volume transport coincided with the subpolar North Atlantic gyre eastern boundary's westward migration and reduced mesoscale activity
- NAC volume transport and heat content increased between 2014 and 2022, which can be propagated into the Atlantic meridional overturning circulation deep branch on decadal timescales

Supporting Information:

Supporting Information may be found in the online version of this article.

Correspondence to:

T. S. Dotto,
tiago.dotto@noc.ac.uk

Citation:

Dotto, T. S., Holliday, N. P., Fraser, N., Moat, B., Firing, Y., Burmeister, K., et al. (2025). Dynamics and temporal variability of the North Atlantic current in the Iceland Basin (2014–2022). *Journal of Geophysical Research: Oceans*, *130*, e2024JC021836. https://doi.org/10.1029/2024JC021836

Received 12 SEP 2024
Accepted 4 JUN 2025

Author Contributions:

Conceptualization: Tiago S. Dotto, N. Penny Holliday
Data curation: Tiago S. Dotto, Yvonne Firing, Darren Rayner
Formal analysis: Tiago S. Dotto, Yvonne Firing, Darren Rayner
Funding acquisition: N. Penny Holliday, Stuart Cunningham, William E. Johns
Investigation: Tiago S. Dotto
Methodology: Tiago S. Dotto, Emma Worthington, William E. Johns
Visualization: Tiago S. Dotto
Writing – original draft: Tiago S. Dotto

Abstract The North Atlantic Current (NAC) is a major source of heat toward the subpolar gyre and northern seas. However, its variability and drivers are not well understood. Here, we evaluated 8 years of continuous daily measurements as part of the international program Overturning in the Subpolar North Atlantic Program to investigate the NAC in the Iceland Basin. We found that the NAC volume and freshwater anomaly transport and heat content (HC) were highly variable with significant variability at timescales of 16–120 days to annual. Intraseasonal to short interannual variability was associated with mesoscale and intermittent mesoscale features abundant in the region. Composites analysis revealed that strong NAC periods were associated with less eddy kinetic energy in the Iceland Basin, which was consistent with the presence of frontal-like structures instead of eddy-like structures. On longer timescales, the westward migration of the eastern boundary of the subpolar North Atlantic (SPNA) gyre favors a stronger NAC volume transport and HC in the region. Stronger zonal wind stress triggers a fast response that piles water up between the SPNA and subtropical gyres, which increases the sea surface height gradient and drives the acceleration of the NAC. The strengthening of the NAC increases the heat and salt transport northward. During our study period, both heat and salt increased across the moorings. These observations are important for understanding the heat and freshwater variability in the SPNA, which ultimately impacts the Atlantic meridional overturning circulation.

Plain Language Summary The Atlantic meridional overturning circulation (AMOC) is a complex system of ocean currents that bring heat poleward and cold/fresh waters equatorward. The North Atlantic Current (NAC), derived from the Gulf Stream, is a major heat source toward the subpolar gyre and northern seas. Here, we evaluated 8 years of daily data measured as part of the international program Overturning in the Subpolar North Atlantic Program. We found that the NAC was highly variable in the Iceland Basin with variability at timescales of 16–120 days to annual. The shorter timescales were associated with eddies propagating with the NAC. Strong NAC was related to periods of strong zonal gradient across the current, less eddy kinetic energy, and with a westward excursion of the eastern boundary of the subpolar North Atlantic gyre. This opened space for warmer water to access the northern environments, such as after 2017. Over 2014–2022, we observed warming and salinification of the upper ocean, which might be a recovery of a period of large freshening in 2015. Our findings are important in understanding the variability of heat that is imported into the subpolar North Atlantic and is modified within the gyre and exported within the AMOC's lower limb.

1. Introduction

The North Atlantic Current (NAC) comprises several branches that cross the North Atlantic transporting large quantities of heat and salt from the western basins of the subtropics poleward (Figure 1a). The NAC originates near the Grand Banks of Newfoundland, derived from the Gulf Stream, and moves approximately 27 ± 5 Sv (in Sverdrups, 1 Sv = 1×10^6 m^3 s^{-1}) eastward across the North Atlantic (Roessler et al., 2015). Heat is lost to the atmosphere on its way north, and the water becomes dense and sinks into deeper depths where it returns southwards carrying cold, relatively fresh and carbon-rich waters equatorward. This complex system of currents, part of the Atlantic meridional overturning circulation (AMOC), regulates the Earth's climate (Lozier et al., 2019).

In the subpolar North Atlantic (SPNA), the moorings deployed as part of the Overturning in the Subpolar North Atlantic Program (OSNAP) capture the variability of three main branches of the NAC (Pollard et al., 2004; Figure 1a). Recent estimates documented a northward flow of 13.2 ± 4.9 (standard deviation) Sv from a NAC branch in the eastern Iceland Basin between July 2014 and July 2018 (Koman et al., 2022), 5.1 ± 3.2 (standard

Writing – review & editing: Tiago S. Dotto, N. Penny Holliday, Neil Fraser, Ben Moat, Yvonne Firing, Kristin Burmeister, Darren Rayner, Stuart Cunningham, Emma Worthington, William E. Johns

deviation) Sv from a branch over the Rockall Plateau (RP) between July 2014 and June 2016 (Houpert et al., 2018), and 4.9 ± 0.6 (standard error) Sv crossing the Rockall Trough (RT) between July 2014 and October 2020 (Fraser et al., 2022). The branches flowing in the Iceland Basin mostly recirculate within the SPNA gyre, whereas the branch that flows within the RT travels further north into the Nordic Seas and Arctic Ocean (Berx et al., 2013; Marsh et al., 2017). From an estimated ~51% of NAC transport that circulates in the SPNA gyre (Petit et al., 2020), ~80% enters the gyre west of RP (Koman et al., 2022). Consequently, changes in hydrography associated with the NAC entering the Iceland Basin could be communicated with the AMOC because the Irminger and Iceland basins are key places for water mass transformation (e.g., Evans et al., 2023; Petit et al., 2020).

The Iceland Basin, and to some extent, the NAC, is dominated by energetic meanders and eddies (Heywood et al., 1994) that can last for months in the region (Shoosmith et al., 2005; Zhao, Bower, Yang, Lin, & Zhou, 2018). Mesoscale processes contribute to about 20% of the total heat transport variability in that basin (Zhao, Bower, Yang, Lin, & Holliday, 2018). The recirculation associated with eddies contributes to reducing the meridional heat transport (MHT) in the Iceland Basin (Zhao, Bower, Yang, Lin, & Holliday, 2018). Barotropic and baroclinic instabilities are associated with the formation and growth of these eddies (Zhao, Bower, Yang, Lin, & Zhou, 2018). On longer timescales, previous studies have shown a decadal variability where periods of warmer and colder conditions (Chafik et al., 2023; D. Desbruyères et al., 2021) are driven by changes in the wind stress (Häkkinen et al., 2011a, 2011b) and the North Atlantic Oscillation (NAO) (Khatri et al., 2022). Warmer (colder) periods are thought to be associated with the contraction (expansion) of the SPNA gyre, which opens (obstructs) pathways for warm and salty subtropical (cold and fresh subpolar) water to access the eastern SPNA (Foukal & Lozier, 2018; Häkkinen & Rhines, 2004; Hátún et al., 2005; Holliday et al., 2020; Koul et al., 2020). Those studies were mostly focused on long (multiyear) timescales. The relation of the strength of the NAC and the SPNA gyre on shorter timescales and the variability of that major current on seasonal and intra-/interannual periods remains to be investigated. Understanding the variability and drivers of the NAC is an important step toward a better comprehension of the AMOC variability and trends and the Atlantification of the Arctic Ocean (Årthun et al., 2019).

In this study, we use the 8 full years (2014–2022) of OSNAP mooring measurements in the Iceland Basin to bring new insights into the variability of the NAC on seasonal, intra-annual, and interannual periods and drivers of the NAC volume transport variability. The paper is structured as follows. Section 2 describes the OSNAP moorings and ancillary data set used to calculate volume, freshwater anomaly, heat and salt transport, and heat and freshwater anomaly content (FWC). The new results associated with a longer time series of OSNAP moorings in the Iceland Basin are described in Section 3. In Section 4, we discuss our findings in the context of previous studies. Our conclusions are described in Section 5.

2. Data and Methods

2.1. Observations

2.1.1. OSNAP Moorings

Three moorings (named IB2, IB3, and IB4) were deployed in the eastern Iceland Basin between July 2014 and July 2022 with a fourth mooring (IB5) added in July 2018 (Figure 1a and Table 1). The moorings were serviced every 2 years. Twelve Seabird MicroCATs SBE37 SMP were installed in IB2, IB3, and IB4 in uneven depths between 50 m depth to the seafloor. For IB5, seven MicroCATs were installed because of the shallower local depth (Table 1). The MicroCATs were synchronized to measure temperature, conductivity, and pressure with 30 min intervals.

The MicroCATs were calibrated against the shipboard CTD by lowering them on casts before deployment and following recovery. Correction coefficients for temperature and conductivity were calculated by examining the average difference between the shipboard CTD and the MicroCATs data. This was done once the instruments were equilibrated (>5 min) and at bottle stop depths greater than approximately 1000 m. Pressure coefficients were determined from the difference found at the deployment depth of the moored MicroCATs. If the depth of the shipboard CTD cast was shallower than the depth at which the MicroCATs were deployed, a least square polynomial extrapolation was then used. The corrections from pre- and post-deployment casts were used to

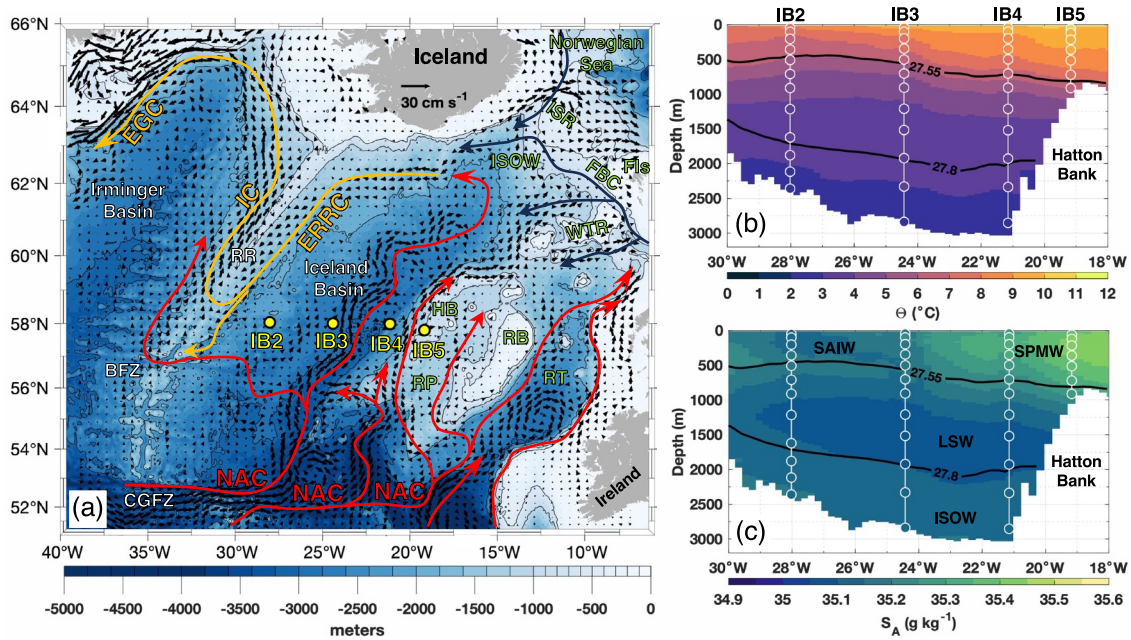

Figure 1. (a) Schematic circulation of the North Atlantic. Black vectors show the time-mean (2014–2022) sea surface geostrophic circulation from satellites. Schematic arrows are color-coded based on the warmer to colder water masses. Mooring (IB2 to IB5) locations are depicted by the yellow dots. Isobaths of 500, 1,000, 2,000, and 3,000 m are depicted by dark gray lines. Bathymetry is shown by the colorbar. Acronyms: Charlie Gibbs Fracture Zone (CGFZ), Bight Fracture Zone (BFZ), Rockall Trough (RT), Rockall Bank (RB), Rockall Plateau (RP), Hatton Bank (HB), Wyville Thomson Ridge (WTR), Faroe Bank Channel (FBC), Faroe Island (FIs), Iceland Scotland Ridge (ISR), Reykjanes Ridge (RR), North Atlantic Current (NAC), Iceland Scotland Overflow Water (ISOW), East Reykjanes Ridge Current (ERRC), Iceland Current (IC), East Greenland Current (EGC). Time-mean OSNAP gridded product (Fu et al., 2023) showing the distribution of (b) conservative temperature and (c) absolute salinity. White circles represent the depth of the MicroCATs on each mooring and time-mean conservative temperature and absolute salinity observed by them. Solid black lines show σ_θ isopycnals. Acronyms in panel (c): Subarctic Intermediate Water (SAIW), Subpolar Mode Water (SPMW), Labrador Sea Water (LSW), and Iceland Scotland Overflow Water (ISOW).

calibrate the MicroCATs with a constant offset or a linear trend. A thorough explanation of the procedure is given by McCarthy et al. (2015).

The time series were 40-hr low-pass filtered using a fourth order Butterworth filter and bin-averaged onto daily intervals. The upper MicroCATs were installed at a nominal depth of 50 m in all moorings. Here, we extrapolated the upper 50 m by combining the data from moorings and satellite sea surface temperature (SST). These ancillary data and the extrapolation method are described next. Due to the shorter period of mooring IB5, the calculations were conducted for the mooring pairs IB2 to IB4 (16 July 2014–22 July 2022) and IB2 to IB5 (5 July 2018–21 July 2022; see Figure 1a for the location of the moorings).

2.1.2. Argo and Remote Sensing

Daily SST product was taken from the Group for High Resolution SST Level 4 analysis (Good et al., 2020). The product combines multiple satellite sensors gridded onto a global 0.05° spatial resolution.

Table 1
Mooring Locations, Period, and Nominal Depths of the MicroCATs Installed in Each Mooring

Mooring	Latitude Longitude	Period	Local depth (m)	Nominal depth (m) of the sensors
IB2	58°02.21′N 28°01.19′W	13 July 2014–27 July 2022	2375	50, 100, 200, 350, 500, 700, 900, 1,200, 1,600, 1,850, 2,080, 2,320
IB3	58°00.32′N 24°24.16′W	15 July 2014–24 July 2022	2844	50, 105, 200, 350, 500, 700, 900, 1,200, 1,500, 1,900, 2,305, 2,800
IB4	57°59.45′N 21°08.72′W	16 July 2014–22 July 2022	2930	50, 105, 200, 350, 500, 700, 900, 1,200, 1,500, 1,900, 2305, 2,800
IB5	57°48.07′N 19°10.26′W	05 July 2018–21 July 2022	942	50, 105, 200, 350, 500, 700, 895

Note. Local depth is estimated from GEBCO (GEBCO 2023 Grid, https://doi.org/10.5285/f98b053b-0cbc-6c23-e053-6c86abc0af7b).

Daily absolute dynamic topography (ADT) Level 4 data were taken from Copernicus Marine Environmental Monitoring Service (CMEMS; DUACS 7.1 baseline DT2021 version vDec2021). The data consist of multi-mission altimeter satellites gridded onto a global 0.25° spatial resolution. For the evaluation of the oceanic conditions during strong and weak NAC volume transport periods, we corrected the ADT for the global mean sea level rise taken as 4.3 mm yr^{-1} for the period (2013–2023; https://climate.copernicus.eu/climate-indicators/sea-level).

2.1.3. Vertical Extrapolation and Gridding

Before gridding the data set, the upper ∼50 m needed to be filled with data. Temperature was extended to the surface by merging the moorings with satellite SST. Following Koman et al. (2022), if the satellite SST was warmer than the upper MicroCAT, the satellite SST was used as the surface end point. Otherwise, the upper MicroCAT temperature measurement was extended to the surface. For salinity, the upper MicroCAT salinity measurement was extended to the surface. This new data set was then interpolated onto a 20 m vertically spaced grid using a piecewise cubic Hermite interpolation scheme to preserve the shape of the profiles. The density field was computed from the new temperature and salinity interpolated data. This procedure guarantees a stable stratification near the surface.

For the vertical extrapolation, we also tested combining the mooring measurement with the Roemmich-Gilson Argo Climatology (Roemmich & Gilson, 2009). In this case, we observed more unstable stratification near the surface, and the final volume transport calculated changed as little as ∼0.14 Sv between methods. Therefore, we decided to use the more straightforward extrapolation consistent with Koman et al. (2022).

2.1.4. Atmospheric Data Set

Hourly mean sea level pressure and zonal and meridional components of the wind were taken from the 0.25-degree spatial resolution ECMWF ERA5 single levels (Hersbach et al., 2020). These were averaged into daily resolutions.

Two NAO indices were combined in this study. Both indices are based on centers of action of 500 mb height patterns using NCEP/NCAR Reanalysis. One index is provided by NOAA/ESRL Physical Science Laboratory and uses the 500 mb height patterns difference between the regions 55°–70°N, 10°–70°W and 35°–45°N, 10°–70°W. The second index is provided by NOAA Climate Prediction Center and it uses a rotated principal component analysis to decompose the 500 mb height anomalies over the North Atlantic region 20°–90°N. We combined the two indices by summing them after they were standardized by their respective standard deviations.

2.2. Geostrophic Velocity, Volume Transport, Heat Content, and Freshwater Content Anomaly

Conservative temperature (Θ), absolute salinity (S_A) and potential density relative to the surface (σ_θ) were calculated from the full-depth daily averaged gridded mooring data (McDougall & Barker, 2011). The horizontal geostrophic velocity shear referenced to the surface was calculated between moorings and integrated upwards for $\sigma_\theta \leq 27.55$ kg m^{-3} and $\sigma_\theta \leq 27.80$ kg m^{-3}. The isopycnal of 27.55 kg m^{-3} marks the upper limb of the AMOC for OSNAP East (Li et al., 2021), and we took this isopycnal to represent the base of the NAC water masses (Figures 1b and 1c). Following Koman et al. (2022), $\sigma_\theta > 27.80$ kg m^{-3} was considered Iceland Scotland Overflow Water and is not included in our estimate for the overall NAC (which in this case, includes Labrador Sea Water (LSW), an old water mass that recirculates in Iceland Basin, Figures 1b and 1c). Sea surface geostrophic velocity (v_{geos}) between moorings was estimated by the ADT difference interpolated into the location of the moorings:

$$v_{\text{geos}} = \frac{g}{f}\left(\frac{\Delta ADT}{x}\right) \quad (1)$$

where g is gravitational acceleration, f is the Coriolis parameter, and x is the distance between moorings in meters. The surface geostrophic velocity calculated from the satellite altimeter was then added to the geostrophic shear from the moorings to give the absolute geostrophic velocity (v_{geos}).

Volume (Sv), heat (PW), salt (kg s^{-1}), and freshwater anomaly (Sv) transports were calculated as

$$\text{Volume transport} = \int \int_{z_{\sigma_\theta}}^{0} v_{\text{geos}} dz\, dx \tag{2}$$

$$\text{Meridional Heat Transport} = \int \int_{z_{\sigma_\theta}}^{0} \rho C_p v_{\text{geos}} \Delta\Theta dz\, dx \tag{3}$$

$$\text{Meridional Salt Transport} = \int \int_{z_{\sigma_\theta}}^{0} \rho S_A v_{\text{geos}} dz\, dx \tag{4}$$

$$\text{Meridional Freshwater Anomaly Transport} = \int \int_{z_{\sigma_\theta}}^{0} v_{\text{geos}} \left(\frac{S_A - S_{\text{ref}}}{S_{\text{ref}}} \right) dz\, dx \tag{5}$$

where z_{σ_θ} is the depth where $\sigma_\theta = 27.80$ kg m^{-3} or $\sigma_\theta = 27.55$ kg m^{-3}, ρ is in situ density, C_p is the specific heat capacity of seawater (taken as 3992 J kg^{-1} K^{-1}), and $\Delta\Theta$ is the observed Θ minus the in situ freezing point. S_{ref} is the time-averaged S_A between moorings for the period 2014–2022 (2018–2022 for IB4 and IB5). The S_{ref} for the mooring pairs IB2–IB3, IB3–IB4, and IB4–IB5 were, respectively, 35.13 g kg^{-1}, 35.16 g kg^{-1}, and 35.22 g kg^{-1} for $\sigma_\theta \leq 27.80$ kg m^{-3}, and 35.18 g kg^{-1}, 35.26 g kg^{-1}, and 35.35 g kg^{-1}, respectively, for $\sigma_\theta \leq 27.55$ kg m^{-3}. A S_{ref} for each mooring pair was used to avoid a high-salinity bias toward the eastern Iceland Basin and to make the anomalies over time comparable. The magnitude of the Ekman transport tends to be an order of magnitude smaller than the total transport (e.g., Houpert et al., 2020); therefore, it is not considered in this study.

Heat Content (J m^{-1}) and FWC (m^2) integrated between moorings were calculated as

$$\text{Heat Content} = \int \int_{z_{\sigma_\theta}}^{0} \rho C_p \Delta\Theta dz\, dx \tag{6}$$

$$\text{Freshwater Anomaly Content} = -\int \int_{z_{\sigma_\theta}}^{0} \frac{\rho(\Theta, S_A, p)}{\rho(\Theta, 0, p)} \frac{S_A - S_{\text{ref}}}{S_{\text{ref}}} dz\, dx \tag{7}$$

2.2.1. Bottom Triangle

The large bottom triangle between IB4 (local depth 2930 m) and IB5 (local depth 942 m) was filled as follows. We assumed that the shear below the deepest common level of the two moorings (900 m) was small (Figure S1 in Supplementary Information S1). This allowed us to extrapolate the deepest velocity of mooring IB5 downwards to 2,000 m, which is the depth where the isopycnal of 27.80 kg m^{-3} reaches the Hatton Bank (HB) (Figure 1b). Between ~900 and ~2,000 m, the distance between the moorings was assumed half according to the triangle area equation. The bottom triangle increased the volume transport by, on average, ~2 Sv. From five LADCP measurements in July 2022, the volume transport through the large bottom triangle was −0.63 Sv (Figure S1 in Supplementary Information S1). By reducing the number of measurements considered and applying our assumption, the volume transport through the bottom triangle increased by almost 1 Sv, and it was estimated at 0.35 Sv. Because LADCP from one cruise is only one realization, we proceed with our assumption for calculating the transport time series while noting the associated uncertainty.

The bottom triangle was dealt with as follows to estimate meridional heat, salt and freshwater anomaly transports, and heat and FWC. Using the OSNAP gridded product (Fu et al., 2023), we evaluated the Θ and S_A profiles between IB4 and IB5 (Figure S2 in Supplementary Information S1). The gridded product profiles tended to converge into the LSW properties (low Θ and S_A) as the IB4 profile. In order to reconstruct a mean profile

between IB4 and IB5, we (a) merged the Θ and S_A from IB4 below the deepest depth measured by IB5, (b) we removed the new data between ∼900 and ∼1,500 m (which coincides with the halocline depth range), and then (c) reconstructed the new Θ and S_A by interpolating the profiles between those depths using a piecewise cubic Hermite interpolation scheme to preserve the shape of the profiles. We used the reconstructed profile up to ∼2,000 m, which coincided with the time-mean depth of the 27.80 kg m^{-3} isopycnal. Finally, for each time step, an averaged profile of Θ and S_A between IB4 and the reconstructed IB5 was used to estimate meridional heat, salt and freshwater anomaly transports, and heat and FWC.

3. Results

3.1. Spatial and Vertical Structure of the NAC

The moorings in the eastern Iceland Basin were deployed to measure two branches of the NAC. A strong geostrophic path of the NAC was observed between the moorings IB3 and IB4 (Figure 1a). In this branch, mesoscale features are frequently seen (e.g., Koman et al., 2022; Zhao, Bower, Yang, Lin, & Holliday, 2018). Their presence was observed on the ocean surface even on a 2014–2022 time-mean altimetry-derived geostrophic velocity (Figure 1a). Another branch steered by the RP's topography, known as the HB Jet (Houpert et al., 2018), crossed IB4 and IB5 in a less-meandering fashion between the 1,000 and 3,000 m isobaths.

The moorings captured the water properties associated with the four main water masses in the region. Subarctic intermediate water occupied the upper ∼500 m between IB2 and IB3. Subpolar Mode Water was present between ∼700 and 900 m between IB3 and IB5. Along the whole section between IB2 and IB5, LSW was present below 1,000 m. Iceland Scotland Overflow Water occupied depths deeper than ∼1,500–2,000 m below 27.80 kg m^{-3} (Figures 1b and 1c).

The 8-year averaged vertical structure of NAC volume, heat, salt and freshwater anomaly transports, and heat and FWC for the eastern Iceland Basin are displayed in Figure 2. The time-averaged volume transport per depth layer was high in the top layers (above 0.4 Sv per 20-m depth bin for the upper 200 m) and reduced to less than 0.1 Sv per each 20-m depth bin below 1,000 m (Figure 2a). Per potential density layers, the data showed two peaks of northward volume transport: an upper peak centered at the isopycnal of ∼27.30 kg m^{-3} and a denser peak centered at ∼27.70 kg m^{-3} (Figure 2b). Low volume transport was found at ∼27.55 kg m^{-3} (Figure 2b), which was the base of the NAC and often described as the delimitation of the upper and lower limbs of the subpolar meridional overturning circulation in the OSNAP East (Li et al., 2021).

The depth-accumulated time-averaged profiles showed stronger northward volume transport in, approximately, the upper 600 and 700 m of the water column for IB2 to IB4 and IB2 to IB5, respectively, which coincided with the depth of the 27.55 kg m^{-3} isopycnal (Figure 2c). The 27.55 kg m^{-3} isopycnal also marked the limit of the warmest and saltiest waters from subtropical origin flowing northward in the eastern North Atlantic near the RP (Figures 1b and 1c). Meridional heat and salt transports were highly dependent on the velocity field and presented a similar structure of the volume transport (Figures 2d and 2f). Given the similarity with volume transport, the time series of meridional heat and salt transports are presented in Figures S3 and S4 in Supplementary Information S1. Freshwater anomaly transport and content resemble each other and are less associated with the velocity field than heat and salt transport. Given the similarities, we present the times series of FWC as supplemental material (Figures S3 and S4 in Supplementary Information S1).

The measurements obtained from IB5 since 2018 captured the warmer variety of the Hatton Jet (Houpert et al., 2018) and showed higher HC for similar depths compared with the section ending at the mooring IB4 (Figure 2g). Meridional freshwater anomaly transport and FWC provide a clear view of the main water masses presented in the region, where the upper layer is characterized by the presence of salty Subpolar Mode Water and less-salty subarctic intermediate water (transporting salt northwards) and the freshwater-rich LSW at intermediate depths (Figures 2e and 2h).

3.2. Temporal Variability, Annual Cycles, and Trends

3.2.1. Water Masses Lighter Than 27.80 kg m^{-3}

The time-average (±1 standard deviation) northward volume transport across IB2–IB4 was estimated at 9.9 ± 4.4 Sv almost doubling to 17.4 ± 3.1 Sv when combined with IB5 (Figures 2c and 3a) (Uncertainties, given

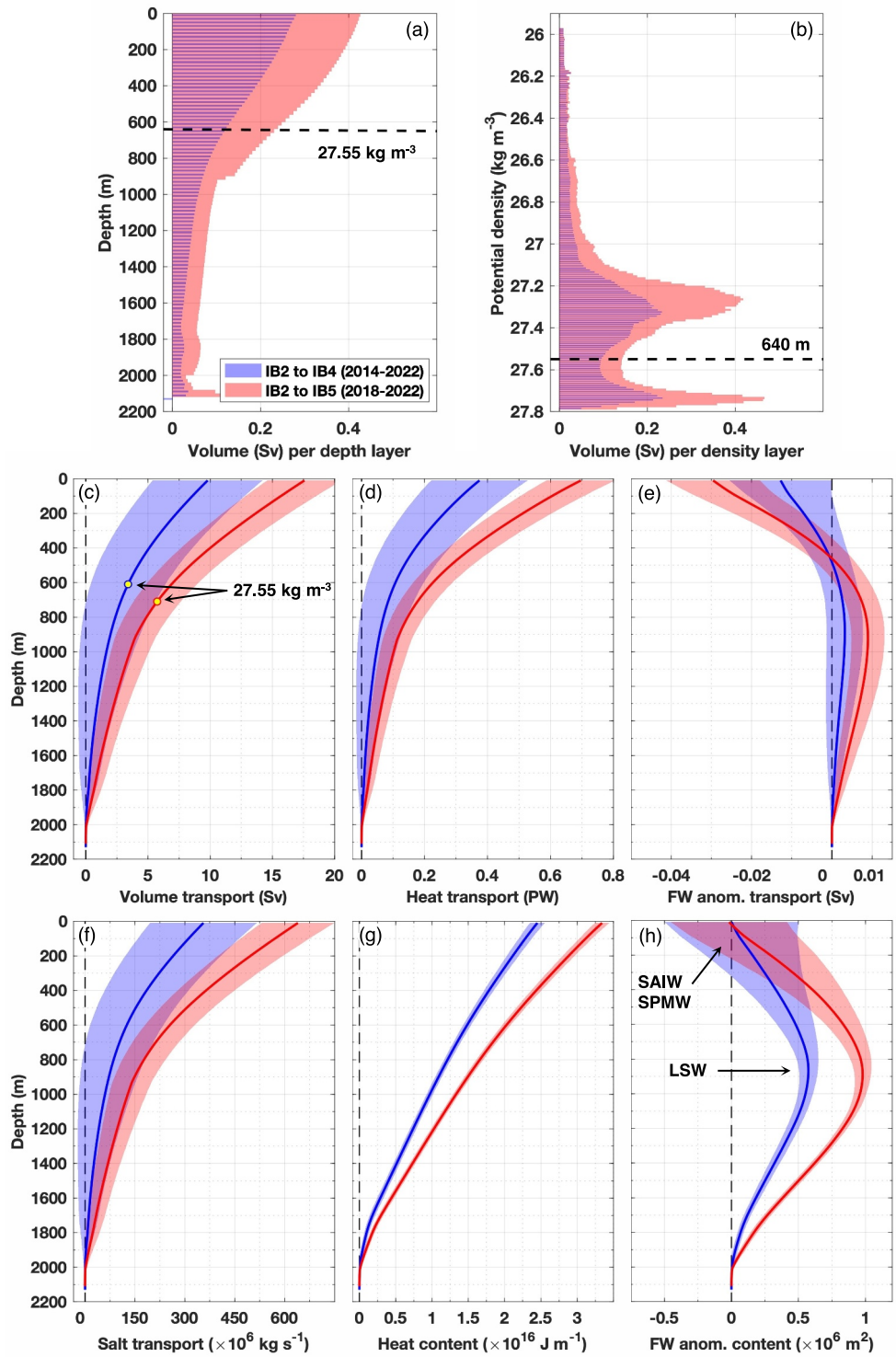

Figure 2. Time-mean profiles of volume transport (a) per depth layer and (b) per potential density layer. Time-mean profiles of (c) volume transport, (d) heat transport, (e) freshwater (FW) anomaly transport, (f) salt transport, (g) heat content, and (h) freshwater (FW) anomaly content integrated from the depth of 27.80 kg m^{-3} to the surface. IB2 to IB4 (IB2 to IB5) is shown by the blue (red) line, and the period considered in the averaging is shown in the legend in panel (a). For panels (c–h), shading represents ±1 standard deviation from the mean. Time-mean depth of 27.55 kg m^{-3} is shown in panel (a). SAIW = Subarctic Intermediate Water, SPMW = Subpolar Mode Water, and LSW = Labrador Sea Water.

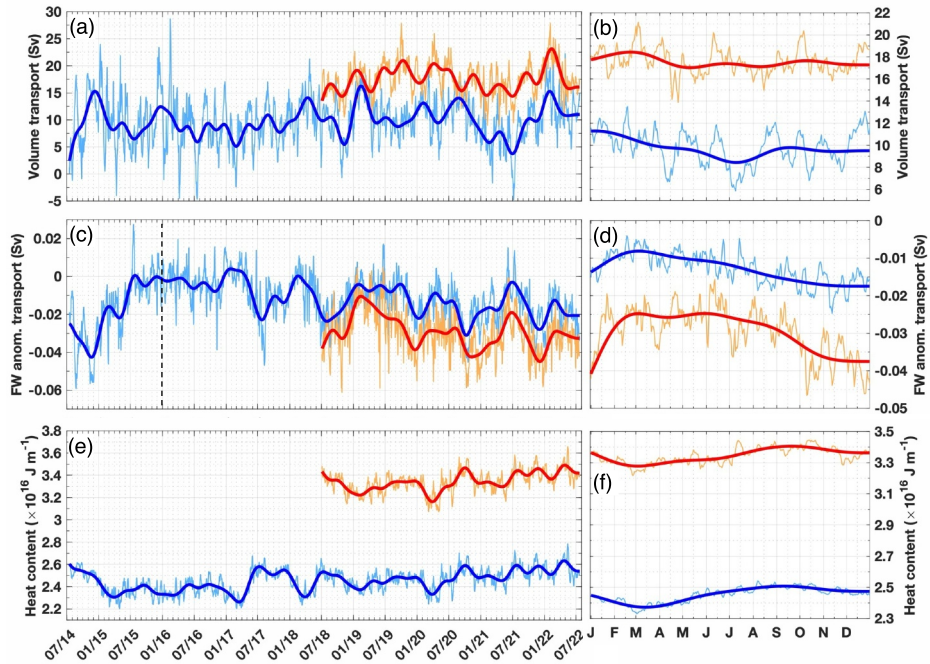

Figure 3. Time series of daily (a) volume transport, (c) freshwater anomaly transport, and (e) heat content integrated from the depth of the isopycnal of 27.80 kg m^{-3} to the surface. IB2 to IB4 (IB2 to IB5) is shown by the blue (red) solid line. Daily annual cycles of the metrics are shown in panels, (b), (d), and (f), respectively. Thick solid line shows the 120-day low-pass filtered time series. Note the different y-axis ranges between full time series and annual cycles. The dashed line in panel (c) shows the time limit used to calculate the trends in freshwater anomaly transport and content.

as standard error from the 40-hr low-pass filtered time series, are presented in Table 2). The 40-hr low-pass filtered time series (called "time series" from here onwards) revealed a high degree of temporal variability with a peak of 28.5 Sv and a minimum of −4.5 Sv for IB2–IB4. For IB2–IB5, the extremes were 27.9 and 9.3 Sv. A 120-day low-pass filter was applied to focus on intra-annual and interannual timescales (called "filtered time series" from here onwards), revealing a range of 14.4 Sv for IB2–IB4 and 9.4 Sv for IB2–IB5. 2021 was marked by a reduction in the volume transport in both IB2–IB4 and IB2–IB5 arrays combination mostly driven by the low volume transport across IB2–IB3 (Figure S5 in Supplementary Information S1). Although one observes an increasing trend in volume transports over time, they were not statistically significant (Table 3). Similarly, meridional heat and salt transport increased over time in both mooring arrays but none was statistically significant.

Table 2
Time-Mean, Standard Deviation and Standard Errors (in Parenthesis) for Volume Transport (Q), Meridional Heat Transport (MHT), Meridional Salt Transport (MST), Meridional Freshwater Anomaly Transport (MFT), Heat Content (HC) and Freshwater Anomaly Content (FWC) Calculated From the Moorings From the 40-hr Low-Pass Filtered Time Series

	IB2 to IB4		IB2 to IB5	
	$\rho_\theta \leq 27.80$ kg m^{-3}	$\rho_\theta \leq 27.55$ kg m^{-3}	$\rho_\theta \leq 27.80$ kg m^{-3}	$\rho_\theta \leq 27.55$ kg m^{-3}
Q (Sv)	9.9 ± 4.4 (0.34)	5.7 ± 1.7 (0.18)	17.4 ± 3.1 (0.36)	10.7 ± 1.5 (0.16)
MHT (PW)	0.38 ± 0.15 (0.01)	0.24 ± 0.08 (0.01)	0.69 ± 0.11 (0.01)	0.48 ± 0.07 (0.01)
MST (x10^6 kg s^{-1})	361 ± 159 (12)	206 ± 63 (7.0)	634 ± 111 (13)	389 ± 55 (6.0)
MFT (Sv)	−0.013 ± 0.013 (0.002)	0.0001 ± 0.011 (0.002)	−0.029 ± 0.012 (0.002)	−0.003 ± 0.010 (0.002)
HC (x10^{16} J m^{-1})	2.45 ± 0.10 (0.02)	0.83 ± 0.15 (0.03)	3.34 ± 0.10 (0.02)	1.28 ± 0.14 (0.03)
FWC (x10^6 m^{-2})	−0.002 ± 0.499 (0.11)	−0.003 ± 0.364 (0.08)	−0.023 ± 0.435 (0.10)	−0.082 ± 0.299 (0.06)

Note. The standard error was calculated as standard deviation divided by the square root of the effective degree of freedom, which is based on the autocorrelation of each time series (Emery & Thomson, 2004).

Table 3
Trends for Volume Transport (Q), Meridional Heat Transport (MHT), Meridional Salt Transport (MST), Meridional Freshwater Anomaly Transport (MFT), Heat Content (HC), and Freshwater Anomaly Content (FWC) Calculated for the Moorings From the 120-Day Low-Pass Filtered Time Series

$\rho_\theta \leq 27.80$ kg m^{-3}						
Moorings	Q (Sv yr^{-1})	MHT (PW yr^{-1})	MST (x10^6 kg s^{-1} yr^{-1})	MFT (Sv yr^{-1})	HC (x10^{16} J m^{-1} yr^{-1})	FWC (x10^6 m^2 yr^{-1})
IB2 to IB4	0.16	0.01	5.81	***0.030*** ***−0.003***	**0.02**	***1.20*** ***−0.11***
IB2 to IB5	0.14	0.01	5.34	**−0.003**	***0.04***	**−0.18**
$\rho_\theta \leq 27.55$ kg m^{-3}						
Moorings	Q (Sv yr^{-1})	MHT (PW yr^{-1})	MST (x10^6 kg s^{-1} yr^{-1})	MFT (Sv yr^{-1})	HC (x10^{16} J m^{-1} yr^{-1})	FWC (x10^6 m^2 yr^{-1})
IB2 to IB4	**0.17**	***0.01***	**6.31**	***0.028*** ***−0.003***	**0.03**	***1.00*** ***−0.10***
IB2 to IB5	0.14	0.01	5.17	−0.003	**0.05**	**−0.11**

Note. For MFT and FWC, the trends were calculated from the beginning of the time series to 1 January 2016 (upper number within the cell) and from 1 January 2016 to the end of the time series (lower number within the cell). Trends in bold depict significance at 95%, and trends in bold and italic are significant at 99%. Statistical significance was based on two-tailed t-tests where the numbers of degrees of freedom were determined from the integral timescale of decorrelation (Emery & Thomson, 2004).

High-frequency variability was visible in the time series when averaged by day of the year (Figure 3b). For the longer time series of the IB2–IB4, an annual cycle is apparent from the filtered time series, where volume transport was reduced in summer (June–July) and increased in winter (December–January). In both mooring arrays combination, the annual cycle of the filtered time series showed a range of ∼2 Sv between maximum and minimum volume transport, which was equivalent to ∼14% and 21% of the range of variability observed across IB2–IB4 and IB2–IB5, respectively.

The time-average meridional freshwater anomaly transport was −0.013 ± 0.013 Sv for IB2–IB4 and −0.029 ± 0.012 Sv for IB2–IB5 (Figure 3c). Recorded peaks were 0.027 and 0.005 Sv, whereas minima were −0.058 Sv and −0.062 Sv for IB2–IB4 and IB2–IB5, respectively. The filtered time series revealed a significant and sharp freshwater anomaly transport increase from late 2014 to late 2015 with a rate of 0.030 Sv yr^{-1} ($p < 0.01$; Table 3). From 2016 to mid-2017, the transport remained high, decreasing thereafter. The linear trend from January 2016 to July 2022 was −0.003 Sv yr^{-1} ($p < 0.01$) for IB2–IB4, and −0.003 Sv yr^{-1} ($p < 0.05$) for IB2–IB5 from July 2018 to July 2022. The annual cycle showed higher meridional freshwater anomaly transport in early spring and lower meridional freshwater anomaly transport in late autumn and early winter more evident in the IB2–IB4 array due to its longer time series (Figure 3d).

The estimated time-mean HC was $2.45 \pm 0.10 \times 10^{16}$ J m^{-1} for IB2–IB4 and $3.34 \pm 0.10 \times 10^{16}$ J m^{-1} for IB2–IB5 (Figure 3e). Maximum values for IB2–IB4 were 2.79×10^{16} J m^{-1}, and minimum values were 2.20×10^{16} J m^{-1}. For IB2–IB5, maximum and minimum values were 3.66×10^{16} J m^{-1} and 3.08×10^{16} J m^{-1}. Over time, HC increased at rates of 0.02×10^{16} J m^{-1} yr^{-1} for IB2–IB4 (July 2014 to July 2022; $p < 0.05$) and 0.04×10^{16} J m^{-1} yr^{-1} for IB2–IB5 (July 2018 to July 2022; $p < 0.01$). Daily HC variability was smaller than subannual to interannual variability. The annual cycle, well captured by both mooring arrays, showed high HC in early autumn and low HC in early spring (Figure 3f).

3.2.2. Water Masses Lighter Than 27.55 kg m^{-3}

For the lighter water class encompassing the NAC, the 8-year averaged volume transport between IB2–IB4 and IB2–IB5 was 5.7 ± 1.7 Sv and 10.7 ± 1.5 Sv, respectively (Figure 4a). Maximum and minimum volume transports for IB2–IB4 were 10.2 Sv and −1.2 Sv, respectively. For IB2–IB5, maximum and minimum values were respectively 15.2 and 6.8 Sv. A deep convection event in March–April 2015 disrupted the water column leading to the observation of waters denser than 27.55 kg m^{-3} in the upper layers of mooring IB2. The filtered time series revealed a negative correlation between volume transport at IB2–IB4 and IB2–IB5 from 2018 to the end of 2020 ($r = -0.54$, $p < 0.01$), becoming positive from 2020 to the end of the record ($r = 0.86$, $p < 0.01$). The volume transport across IB2–IB4 increased at a rate of 0.17 Sv yr^{-1} over time ($p < 0.05$; Table 3) for the filtered time series. The annual cycle became evident after 4 years of data (Figure 4b). High volume transport was seen in

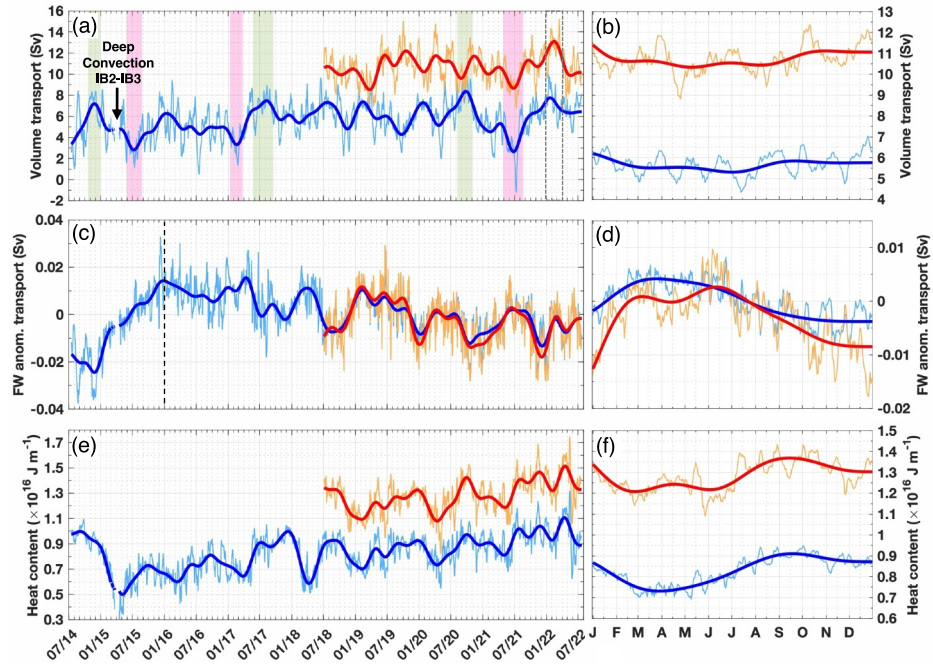

Figure 4. Time series of daily (a) volume transport, (c) freshwater (FW) anomaly transport, and (e) heat content integrated from the depth of the isopycnal of 27.55 kg m^{-3} to the surface. IB2 to IB4 (IB2 to IB5) is shown by the blue (red) solid line. Daily annual cycles of the metrics are shown in panels, (b), (d), and (f), respectively. Thick solid line shows the 120-day low-pass filtered time series. Note the different y-axis ranges between full time series and annual cycles. Green (pink) rectangles in panel (a) show periods of high (low) volume transport captured by IB2 to IB4 and used to create Figure 5. The dashed rectangle in panel (a) shows the period when IB2–IB5 was the strongest. The gap in the time series in March–April 2015 is due to a deep convection event between IB2 and IB3. The dashed line in panel (c) shows the time limit used to calculate the trends in freshwater anomaly transport and content.

autumn and winter and low volume transport was observed in spring and summer (Figure 4b). The range of volume transport in the filtered time series was ∼1 Sv smaller than the high-frequency variability.

Maximum and minimum freshwater anomaly transport were, respectively, 0.033 Sv and −0.038 Sv for IB2–IB4, and 0.029 and −0.028 for IB2–IB5 (Figure 4c). Notable features include a rapid increase in freshwater anomaly transport from July 2014 to December 2015 (0.028 Sv yr^{-1}, $p < 0.01$) and a subsequent decreasing trend (−0.003 Sv yr^{-1}, $p < 0.01$) from January 2016 onwards in IB2–IB4 (Table 3). The annual cycle revealed higher freshwater anomaly transport in spring and early summer contrasting with lower values in late autumn and winter (Figure 4d).

The time-mean HC measured by the moorings were $0.83 \pm 0.15 \times 10^{16}$ J m^{-1} for IB2–IB4 and $1.28 \pm 0.14 \times 10^{16}$ J m^{-1} for IB2–IB5 (Figure 4e). Maximum HC peaked at 1.32×10^{16} J m^{-1} and minimum at 0.30×10^{16} J m^{-1} for IB2–IB4. For IB2–IB5, the maximum and minimum were, respectively, 1.75×10^{16} J m^{-1} and 0.83×10^{16} J m^{-1}. The linear trends revealed increasing HC at rates of 0.03×10^{16} J m^{-1} yr^{-1} and 0.05×10^{16} J m^{-1} yr^{-1} (both $p < 0.05$) for IB2–IB4 and IB2–IB5, respectively (Table 3). Both arrays exhibited an annual cycle with high HC peaking in autumn and low HC in spring (Figure 4f).

Next, we used wavelet analysis (Grinsted et al., 2004) to identify the dominant periods and years of higher variability in the volume and freshwater anomaly transports and HC from the time series. The wavelet analysis was carried out from the 18th of April 2015 to the end of our time series to avoid the data gap caused by the deep convection event (Figure 4a). A significant variability in the volume transport was identified ranging from ∼16 to ∼120-day period in both IB2–IB4 and IB2-IB5 (Figures 5a and 5b). This range of frequencies was present almost all times during the years analyzed, showing the dominance of the signal in the mooring location. High energy at ∼64–120-day periods was observed in the IB2–IB4 at the beginning and at the end of the time series; whereas for IB2–IB5, there was high energy in those periods in 2019 and 2020 (years when the volume transport time series are anticorrelated). The freshwater anomaly transport had a marked energy peaking at annual periods with higher

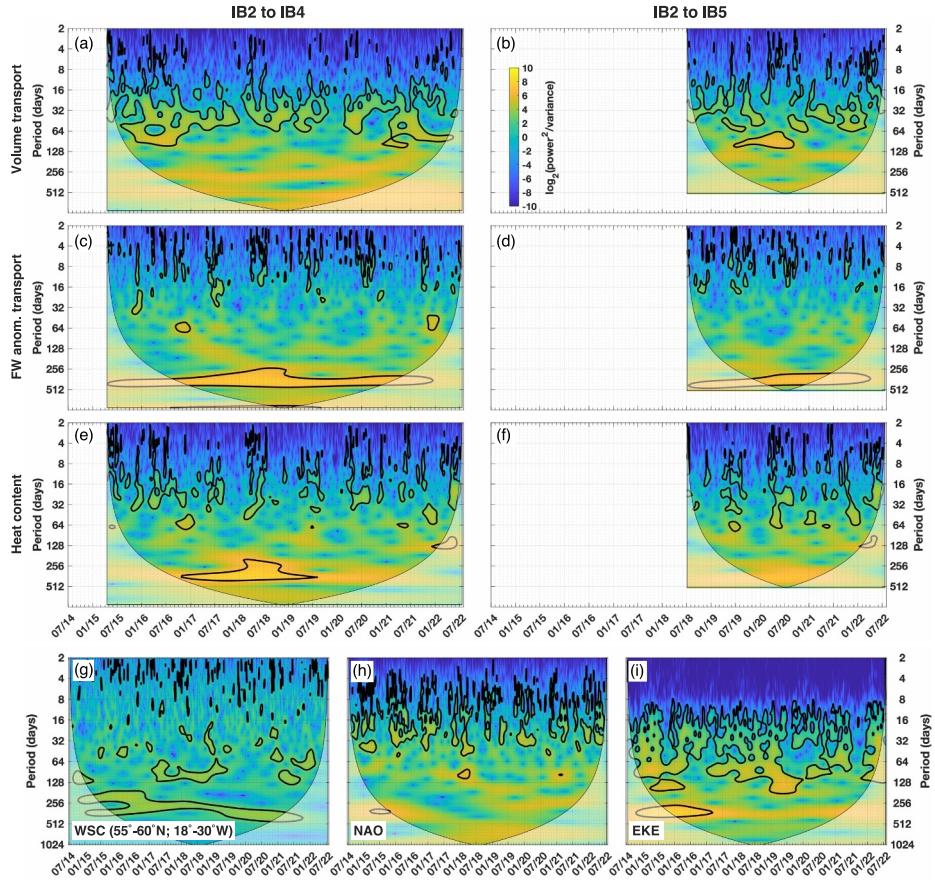

Figure 5. Continuous wavelets analysis (Grinsted et al., 2004) for (a) IB2–IB4 and (b) IB2–B5 volume transport, (c) IB2–IB4 and (d) IB2–IB5 meridional freshwater anomaly (FW anom.) transport, (e) IB2–IB4 and (f) IB2–IB5 heat content, (g) wind stress curl calculated within the region averaged within the area 55°–60°S and 18–30°W, (h) North Atlantic Oscillation and (a) eddy kinetic energy ($EKE = \frac{u'^2 + v'^2}{2}$) along the mooring array. The time series were detrended and standardized by their respective standard deviation before the computation of the wavelets. The black contours depict the 95% significance level. The cone of influence is shown by the lighter shade.

frequency energy occurring in sporadic years. Conversely, the HC time series showed significant variability within 16–64 days (occurring mainly in summer seasons) and on annual periods (Figures 5c–5f).

To better relate those signals of variability with forcings, we evaluated wavelets of wind stress curl (WSC), NAO index, and eddy kinetic energy (EKE) around the moorings. The WSC (taken as the average within the area 55°–60°S and 18–30°W) showed a marked signal at annual periods (Figure 5g). Although higher frequencies could be identified in the time series, they were sporadic. The NAO showed significant energy at periods <30 days mostly concentrated during the winter months (Figure 5h). Finally, the EKE (averaged over the array) showed significant energy between 16 and 120 days most of the time during our study period (Figure 5i). The similarity in frequency periods between EKE and the volume transport suggests that mesoscale features might have an important role in driving the variability of the NAC volume transport across the array of those short timescales.

3.3. Oceanic and Atmospheric Conditions During Strong and Weak NAC Transport

In the previous section, we showed that the clearest signal regarding seasonality and trends are associated with the lighter layers of the NAC, that is, $\sigma_\theta \leq 27.55$ kg m^{-3}. Therefore, we selected the three strongest and weakest periods of the lighter layers of NAC volume transport from the longest IB2–IB4 record and for the peak volume transport in IB2–IB5 (Figure 4a) to look for evidence of drivers. We analyzed sea surface height, EKE, and surface geostrophic velocity.

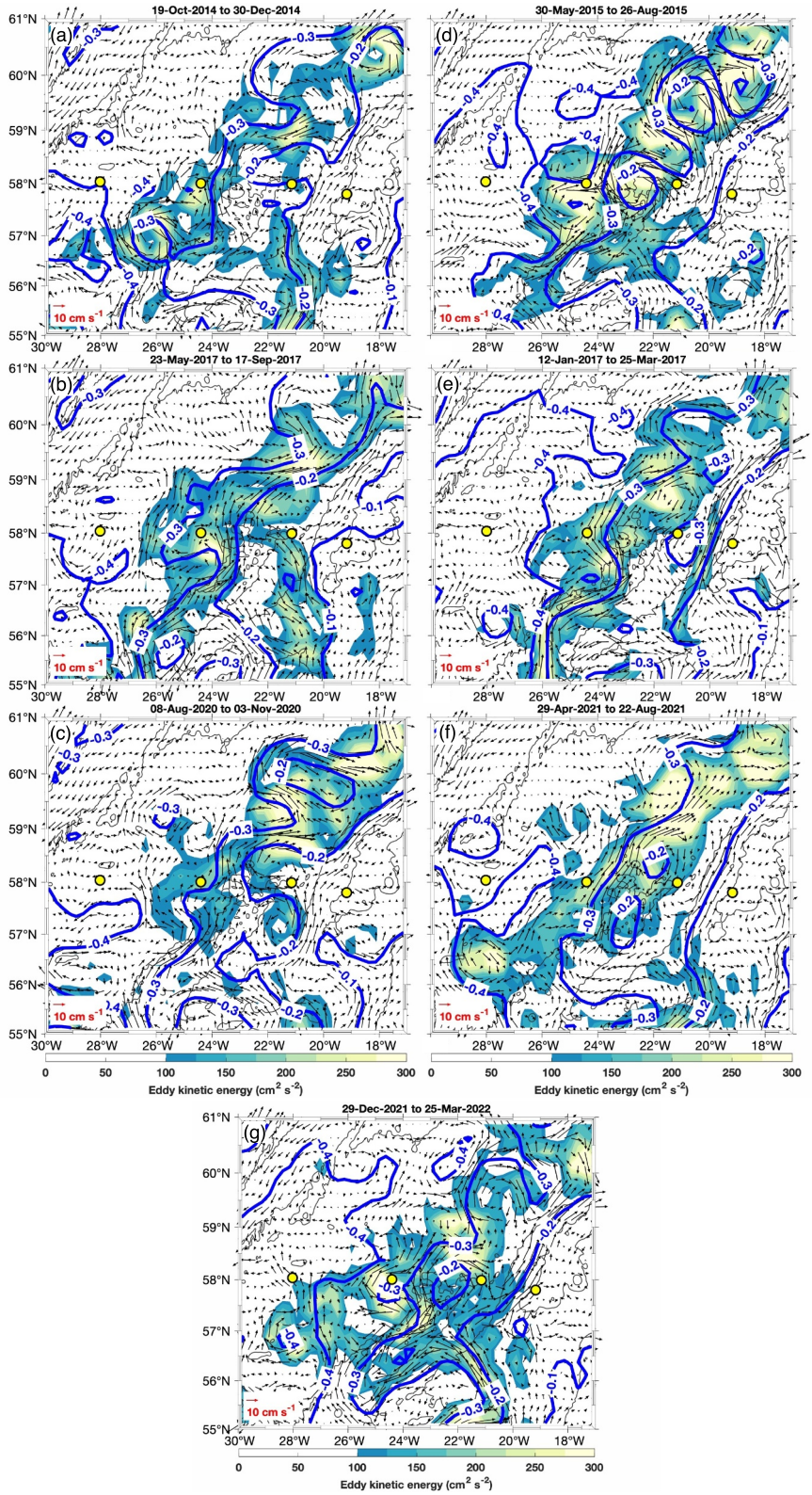

Figure 6.

During the strong NAC volume transport periods from the IB2–IB4 time series, the sea surface isolines of −0.3 m and −0.2 m were closer to each other between IB3 and IB4, which increased the local zonal gradient of sea surface height, resulting in intensified ocean currents there (Figures 6a–6c). Mesoscale features were characterized by their centers near the mooring IB4, and then only the northward flow was captured by the IB2–IB4 time series (Figures 6a–6c and Figure S6a in Supplementary Information S1). We also note a reduction in the regional EKE, calculated as the averaged difference between strong and weak periods over the array section, by ∼41 $cm^2\ s^{-2}$ compared with the period of the three weakest NAC volume transport.

During the weak NAC volume transport periods from the IB2–IB4 time series, the sea surface height isolines of −0.3 m and −0.2 m were further apart from each other, which reduced the zonal gradient of the sea level (Figures 6d–6f). Mesoscale features were more common during those weak periods near the mooring IB3 (Figure S6b in Supplementary Information S1) evidenced by the regional increase in the EKE. These features, which characterize the presence of mesoscale anticyclonic eddies across the mooring array or mesoscale cyclonic eddies near IB4, generated returning flows through IB3 and IB4 reducing the overall NAC volume transport (Figure S6b in Supplementary Information S1).

We also note that the volume transport in IB2–IB5 was high between the 29th December 2021 and 25th March 2022 (Figure 4a). This was caused by a combination of strong flow between the segments of IB2–IB3 and IB4–IB5 (Figure 6g and Figure S5 in Supplementary Information S1). Between IB3–IB4, there was an anticyclonic mesoscale feature that reversed the flow near IB4 (Figure 6g) reducing the overall volume transport in that segment (Figure S5 in Supplementary Information S1).

These maps revealed that mesoscale features not only act on intraseasonal timescales but also on short interannual timescales. Two main patterns in the ocean conditions near the mooring array were identified: a frontal system was observed during the strong volume transport periods, and there was a presence of mesoscale features that may control the variability of the NAC by reversing the flow between IB3 and IB4. Intermittent eddies in the region could be a plausible explanation for driving the variability of the NAC (e.g., Zhao, Bower, Yang, Lin, & Zhou, 2018, Zhao, Bower, Yang, Lin, & Holliday, 2018).

We now investigate further the variability of the sea surface height on the mooring array and its relation to volume transport and HC (Figure 7). Figures 7a and 7b show a clear relationship between an increase in the sea surface height and an increase in the volume transport and HC. The NAC volume transport showed a significant positive correlation with the sea surface height nearly above IB4 (Figure 7c), and it also showed a significant positive correlation with the sea surface geostrophic velocity west of IB4 and a significant negative correlation east of IB4 (Figure 7d). The correlation patterns agree with the presence of anticyclonic mesoscale features that might control the variability of the volume transport through the array. This agrees in part with the wavelet analysis that showed evidence that mesoscale processes control much of the intraseasonal (Figure 5) but also adds that intermittent mesoscale features can also control the NAC volume transport on short-term interannual timescales at the mooring array as discussed previously.

Next, we examined the large-scale North Atlantic changes in the ocean and atmosphere associated with all periods when the NAC volume transport was one standard deviation above or below the mean value of the detrended filtered time series (Figure 8a). The number of occurrences of the events did not show a seasonal bias (Figure 8b), which suggests that the changes in the NAC transport are not dependent on changes in the seasonality of the gyre (e.g., Foukal & Lozier, 2017). Composites based on high and low transport periods were created for the 120-day low-pass filtered sea surface height and the 120-day low-pass filtered EKE, and the difference between them (i.e., high minus low) are presented in Figures 8c and 8d.

The zonal gradient of the sea surface height was elevated during high NAC volume transport periods, that is, the sea surface height was partially reduced in the center/western boundary of the SPNA gyre and elevated on the eastern boundary (Figure 8c). Additionally, the sea surface height isolines (e.g., −0.3, −0.2 and −0.1 m) at the

Figure 6. Mean sea surface height (m, blue solid lines), surface geostrophic velocities (cm s^{-1}, black arrows), and eddy kinetic energy (EKE) ($cm^2\ s^{-2}$, colorbar) for periods of strong (a–c) and weak (d–f) North Atlantic Current volume transport as identified from the detrended time series in Figure 4a. (g) Mean sea surface height, surface geostrophic velocities, and EKE for the period of strong IB2–IB5 volume transport marked by a dashed rectangle in Figure 4a. EKE lower than 100 $cm^2\ s^{-2}$ is masked in white. Yellow dots depict the location of the moorings IB2 (left) to IB5 (right). Dark gray lines depict isobaths of 1,000, 2,000, and 3,000 m. Trends were removed from the data sets before averaging.

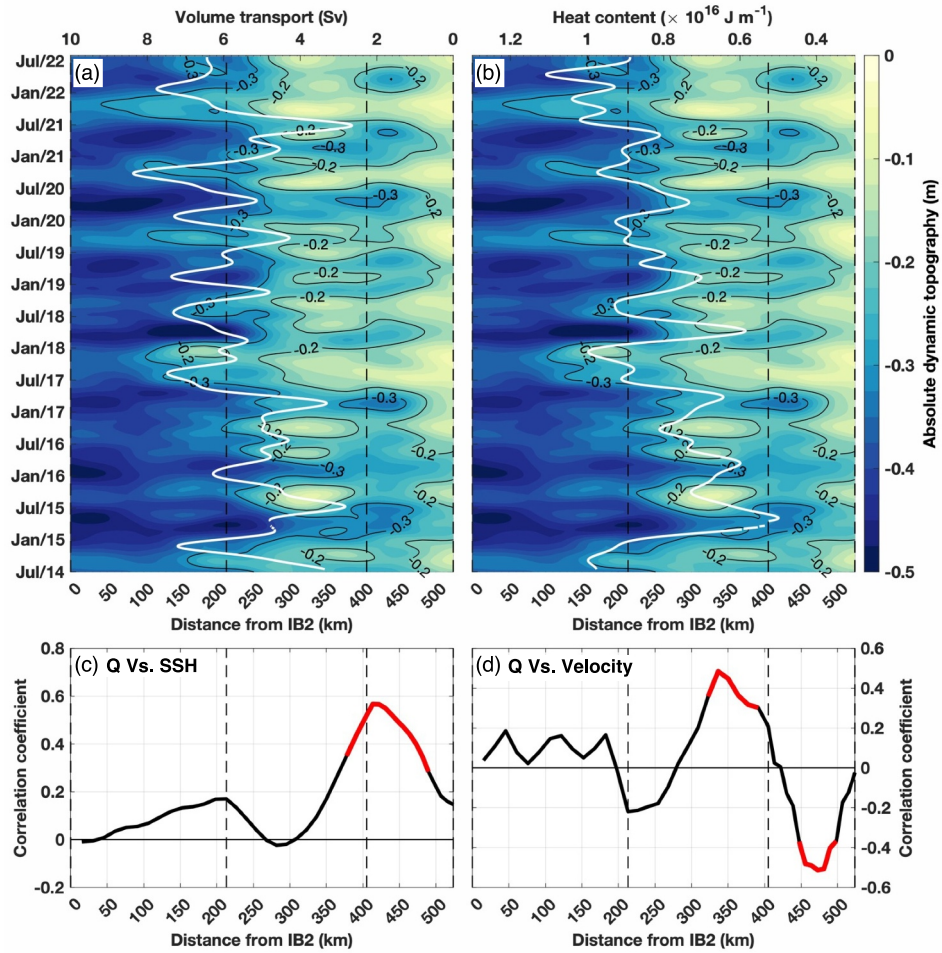

Figure 7. Relationship between the North Atlantic Current (NAC) volume transport and Heat Content (HC) and the sea surface height on the mooring array. Hovmoller diagrams of absolute dynamic topography (ADT) (m) between IB2 and IB5 and the (a) volume transport (Sv) and (b) HC (both showed in solid white line) estimated between IB2–IB4 for $\sigma_\theta \leq$ 27.55 kg m^{-3}. Correlation coefficient between the NAC volume transport estimated between IB2–IB4 for $\sigma_\theta \leq 27.55$ kg m^{-3} and the (c) ADT and (d) sea surface geostrophic velocity. In panels c and d, the red line shows the 95% significance level. Dashed vertical lines are the locations of the moorings IB2, IB3, IB4, and IB5.

eastern boundary of the gyre moved westward. The proximity of the sea surface isolines, for example, −0.3 and −0.2 m, during the strong NAC volume transport periods, generated a frontal structure that intensified the current via stronger zonal gradients. Additionally, the sea surface height difference between high and low NAC volume transport showed an anticyclonic feature over the mooring IB4. This might indicate the presence of intermittent eddies intensifying the flow between IB3–IB4 on short interannual periods. These analyses also revealed a reduction of the EKE along the pathway of the NAC crossing the North Atlantic (Figure 8d), which could indicate a less meandering flow during the strong NAC periods or a more developed train of eddy-like structures between the relaxed sea surface height isolines during the weak NAC periods.

The difference between strong and weak NAC periods for the atmospheric field showed negative WSC south of ∼57°N and positive WSC north of ∼57°N (Figure 8e). This was associated with the positive mean sea level pressure anomaly south of ∼53°N and negative mean sea level pressure anomaly north ∼53°N. This induced, geostrophically, an eastward zonal wind stress anomaly over the North Atlantic (Figure 8e). The result was an equatorward Ekman transport displacing water from the SPNA gyre and pilling it at the northern subtropical region, a region known as "intergyre-gyre" (Marshall et al., 2001). This is consistent with the sea surface height changes described before.

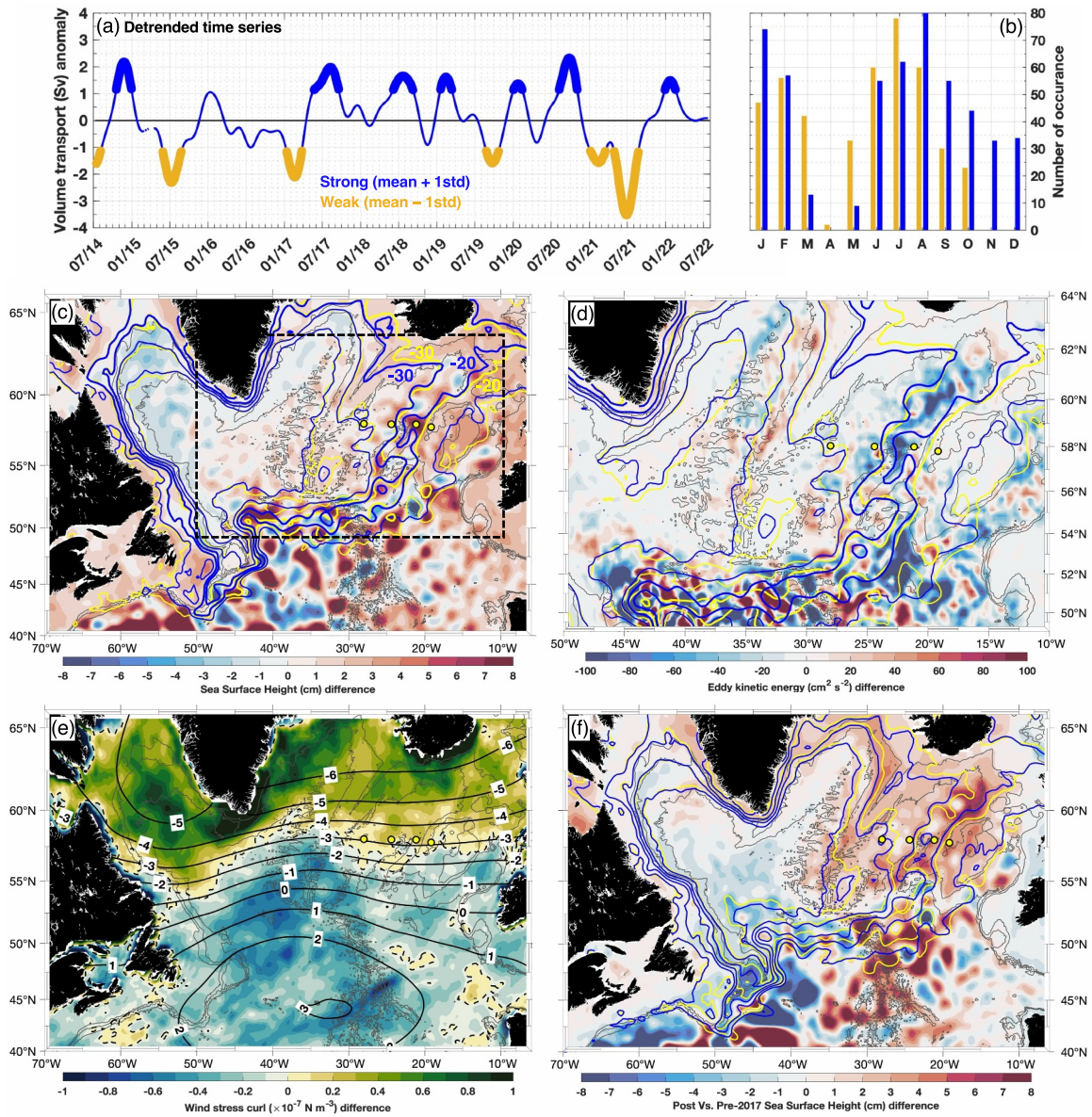

Figure 8. Ocean and atmospheric changes during strong and weak North Atlantic Current periods. (a) Detrended and demeaned time series of volume transport between IB2–IB4 for $\sigma_\theta \leq 27.55$ kg m^{-3} used to calculate the composites. Blue marks the periods of high transport, and orange marks the periods of low transport. (b) Seasonal distribution of high and low transport. (c) Composite difference (high minus low) of sea surface height (cm) for periods of high (blue) and low (yellow) volume transport. The thin blue and yellow lines show the absolute dynamic topography (ADT) every 10 cm for periods of high and low volume transport, respectively. Thick lines depict the values of −30 and −20 cm. The dashed rectangle shows the area plotted in panel (e). (d) Eddy kinetic energy (cm^2 s^{-2}) difference between high and low volume transport periods. Blue and yellow lines follow panel (c). (e) wind stress curl (WSC) (N m^{-3}) difference between high and low volume transport periods. The dashed black line shows the zero WSC. The solid black lines show the mean sea level pressure (hPa) difference between the periods. For panels (c–e), the trends were removed from the data sets before averaging. (f) Sea surface height (cm) difference between post-2017 and pre-2017. The blue and yellow lines show the ADT every 10 cm for periods of post-2017 and pre-2017, respectively. The dark gray lines depict the isobaths of 1,000, 2,000, and 3,000 m.

The spatial displacement of the sea surface height isolines (Figure 7) and the longer interannual variability associated with the NAC (Figure 4) could also reflect a large-scale change in the North Atlantic, such as the expansion and contraction of the SPNA gyre. There is a noticeable relationship between changes in the eastern boundary of the gyre and the NAC volume transport (Figure 7a). For instance, the period between 2014 and 2017 was marked by a low volume transport relative to post-2017. This mechanism of expansion and contraction of the SPNA gyre is evidenced by comparing the sea surface height pre-2017 and post-2017 (Figure 8f). During those early years, the sea surface height was reduced at the location of the mooring array, which could be an indication

of an expansion of the SPNA gyre (Figure 7a). Looking at the larger scale North Atlantic, the SPNA gyre was indeed larger before 2017 than after 2017 (Figure 8f). The transition between small and large gyre was well captured in Figure 7a, which also showed a step-like change in the volume transport between January and July 2017. Before 2017, the isoline of −0.2 m was reaching areas above the HB. After 2017, the same isoline was always located westward of the IB5. Therefore, these analyses suggest that the large-scale adjustment of the gyre, through changes in the sea surface height within the gyre and at its boundary, also influences the NAC volume transport over longer timescales than the mesoscale features described before.

4. Discussion

Our time-mean volume transport observations were consistent with previous measurements in the Iceland Basin (e.g., Bacon, 1997; Koman et al., 2022; Sarafanov et al., 2012; Aken & Becker, 1996). Sarafanov et al. (2012) estimated a northward volume transport of 6.0 ± 0.6 Sv for layers $\sigma_\theta \leq 27.55$ kg m^{-3} and 5.3 ± 1.2 Sv for layers 27.55 kg m^{-3} $< \sigma_\theta \leq$ 27.80 kg m^{-3} at the eastern Iceland Basin across 59.5°N from summer hydrography in combination with satellite altimetry between 2002 and 2008. More recently, Koman et al. (2022) reported a mean (±1 standard deviation) northward transport of 13.2 ± 4.9 Sv through IB2 and IB4 ($\sigma_\theta \leq 27.80$ kg m^{-3}). Our work extended the volume transport time series between IB2 and IB4 presented by Koman et al. (2022) and has added the mooring IB5 to capture the second branch of the NAC in the Iceland Basin (Figure 1). The variability in the time series between IB2 to IB4 by Koman et al. (2022) is consistent with our results, and we observed similar time-mean volume transport when using the same CMEMS altimetry product as those authors (i.e., DUACS 6.1 version 4.0.0) to reference our geostrophic velocities (not shown). Therefore, the ∼3 Sv difference between the time-mean volume transports was associated with the new CMEMS satellite product. Although the new altimetry-derived geostrophic velocity product correlated better with moored acoustic doppler current profiler in the subpolar region than the older version (e.g., Hansen et al., 2023), the lack of consistency regarding the time-mean volume transport between products is a source of uncertainty. More efforts are needed to investigate further the causes of this difference but that was beyond the scope of this work.

The NAC in the Iceland Basin was highly variable on timescales from days to months. Significant variability was observed on 16–120-day periods for the volume transport up to annual periods when considering freshwater anomaly transport and HC (Figure 5). Although the latter indicates the annual cycle of the properties, the former variability is likely due to mesoscale features (Figure 5i) that are often present in the Iceland Basin (e.g., Heywood et al., 1994; Shoosmith et al., 2005; Zhao, Bower, Yang, Lin, & Zhou, 2018, Zhao, Bower, Yang, Lin, & Holliday, 2018; Kondetharayil Soman et al., 2022). Our analysis revealed that the EKE is high when the NAC volume transport was weak, which is consistent with Zhao, Bower, Yang, Lin, & Holliday (2018) conclusion that mesoscale eddies were responsible for decreasing the MHT due to the associated return flux. Note that volume transport and MHT were highly similar in our analysis (compare Figures 3 and 4 with Figures S3 and S4 in Supplementary Information S1). A higher presence of long-lasting eddies crossing the mooring array could indicate a weak NAC and high EKE (Figure 6). Also in agreement with Zhao, Bower, Yang, Lin, and Holliday (2018) and Houpert et al. (2020), the high volume transport associated with the NAC was observed on frontal systems, that is, when the sea surface height isolines are closer and the zonal gradient was stronger, developing strong jets.

The annual cycle observed from our filtered time series was relatively small potentially due to the large variability associated with the mesoscale field. The amplitude of the filtered time series was about 1 Sv for waters lighter than 27.55 kg m^{-3} and 2 Sv for waters lighter than 27.80 kg m^{-3}; whereas, for the RT, it can reach values around 3 Sv or more (Fraser et al., 2022; Houpert et al., 2020). Despite the low amplitude found in our analysis, the seasonality of the volume transport in the Iceland Basin was consistent with the trans-basin transports measured between Portugal and Greenland, which showed high volume transport in autumn and winter and low volume transport in late spring and summer (Mercier et al., 2015; although the updated seasonal cycle presented by Mercier et al. (2024) showed maximum and minimum volume transport in early spring and late summer). Conversely, the phasing of the seasonal cycle of the NAC volume transport at the eastern Iceland Basin was slightly different from the branches at the RT. In the RT, the seasonality of the NAC was maximum in spring and autumn and minimum in summer and winter (e.g., Fraser et al., 2022; Gary et al., 2018; Houpert et al., 2020). An anticorrelation between the sea surface height in the Iceland Basin and RT has been shown before (Chafik et al., 2014) but the reasons still need to be investigated. The differences in the timing of the annual cycle between the sides of the RP suggest that different forcings, potentially local, drive the branches of the NAC. We note that the branches within the Iceland Basin also might respond to different forcings as seen by the period between 2018 and 2020 (Figure 4).

The atmospheric pattern associated with periods of strong NAC resembled a positive phase of the NAO (Figure 8e). The NAO is known to influence the SPNA on short (few months) and longer (>2–3 yr) timescales (e.g., Khatri et al., 2022). On short timescales, the strengthened zonal wind on the subpolar region (Eden & Willebrand, 2001) induces a southward Ekman transport, cooling within the SPNA gyre region, and strengthening and eastward expansion of the SPNA gyre (Khatri et al., 2022; Koul et al., 2020; Lohmann et al., 2009; Roussenov et al., 2022). Our composite analyses differ from those results by showing instead a westward migration of the eastern boundary of the SPNA gyre during the positive NAO-like period. This is a picture more in line with Häkkinen et al. (2011a, 2011b) and Foukal and Lozier (2017) where reduced WSC in the SPNA is associated with a smaller gyre and northward penetration of subtropical waters. The subtropical waters reached the SPNA through the intensification of the NAC during which a frontal system was formed (Figures 7 and 8). The NAC was intensified by a fast adjustment driven by the southward Ekman transport converging and piling water up at the "intergyre-gyre" region, elevating the sea surface height and barotropically increasing the transport of the NAC (Figure 8). One cannot rule out, at least partially, an intensification of the SPNA gyre since the NAC composes its eastern boundary. The atmospheric pattern suggests that the "intergyre-gyre" region tended to circulate anti-cyclonically (Figure 8e), agreeing with Marshall et al. (2001), and favoring the volume, meridional heat and salt transports into the eastern SPNA. This process is clearer on longer timescales (Figure 7), whereas eddies and intermittent eddies near IB4 might be responsible for driving the variability on intraseasonal and shorter inter-annual periods (Figures 5 and 6).

Our time period covered the end of the largest freshening event in 120 years in the eastern SPNA (Holliday et al., 2020) and the temporal evolution of it afterward. The cold and fresh signals from the SPNA gyre peaked in the eastern Iceland Basin in early 2016 (Figures 3 and 4). This early period coincided with an eastward expanded SPNA gyre and low NAC volume transport (Figures 7a and 7b) (This is opposite to the RT, which showed high volume transport during 2014/2015, see Figure 9 of Fraser et al., 2022). Once the fresh and cold period ended, the eastern boundary of the SPNA gyre migrated westward opening pathways for NAC to fully access the region, transitioning into a period of high volume transport, high heat and salt content (Figures 3, 4 and 7). A stronger inflow of NAC carried more heat and salt northwards into the SPNA gyre, as observed from 2017 to the end of our study period (Figures 3 and 4 and Table 1).

The positive trends of 0.17 Sv yr^{-1} for the volume transport and 0.03×10^{16} J m^{-1} for the HC, taken from the filtered time series (Table 3), since 2014 agreed with the new SPNA warming phase described by D. Desbruyères et al. (2021) and Chafik et al. (2023). These studies showed that there has been an increased volume of subtropical water entering the eastern SPNA since 2016 due to adjustment of the NAC derived from southward propagation of deep density anomalies from the Labrador Sea, which strengthened the horizontal circulation and the MHT (Chafik et al., 2023). The spread of the heat and salt signals westwards toward the SPNA gyre, with a time-lag of ∼2 years between the eastern SPNA and the Irminger Sea (e.g., Biló et al., 2022), has the potential to impact the density structure and water mass transformation at the boundary currents (Evans et al., 2023; Petit et al., 2020). More subtropical water entering the SPNA gyre may lead to a higher upper ocean heat loss, more densification and an increase in the AMOC strength (Megann et al., 2021). However, there is a time lag of around 5–10 years for the surface properties to propagate downward to dense water layers (e.g., D. G. Desbruyères et al., 2020). Therefore, the continuation of the OSNAP measurements is key to fully understanding the relationship between NAC and the AMOC on those timescales.

5. Conclusions

Here, we presented new observations of the NAC variability from continuous 8-year OSNAP measurements at the eastern Iceland Basin. Volume and freshwater anomaly transports and HC were calculated for the full ($\rho_\theta \leq$ 27.80 kg m^{-3}) and upper ($\rho_\theta \leq$ 27.55 kg m^{-3}) NAC. We showed that the NAC had a significant variability between 16 and 120-day periods, which was associated with mesoscale features in the Iceland Basin. Intermittent mesoscale features near IB4 also played a role in driving the variability of the volume transport between IB2–IB4 on short interannual timescales. On longer timescales (longer than interannual), we showed that periods of strong and weak NAC coincide with zonal migrations of SPNA gyre eastern boundary. Strong NAC was associated with a westward shift of the eastern boundary of the SPNA gyre, less meanders and EKE, which reflected a frontal system (Zhao, Bower, Yang, Lin, & Holliday, 2018). The large-scale gyre adjustment seemed to be related to wind forcing, which resembled a positive phase of the NAO. Zonal winds piled water up rapidly at the "intergyre-gyre" region, which drove a gradient in the sea surface height and forced the strengthening of the NAC. This

resulted in a larger volume of subtropical waters reaching the Iceland Basin (mainly after 2017) contributing to higher meridional heat and salt transports. The seasonal cycle of the NAC in the Iceland Basin was small, and the time of the peaks was different than the RT, which suggests that local forcing might play a role in driving the different branches of the NAC. Finally, the NAC time series showed a positive trend in the volume transport and HC. Although relatively small, these trends might be translated into the AMOC in the next few years. The OSNAP array completed 10 years in 2024 since deployment, which is the upper bound time lag estimated for surface signals to propagate into the deep ocean in the SPNA. Therefore, a continuation of the OSNAP is highly necessary to properly observe the relationship between the NAC and AMOC on different timescales.

Conflict of Interest

The authors declare that they have no conflict of interest.

Data Availability Statement

Sea surface temperature is available at https://cds.climate.copernicus.eu/datasets/satellite-sea-surface-temperature?tab=overview (Copernicus Climate Change Service, 2019). Absolute dynamic topography is available at https://data.marine.copernicus.eu/product/SEALEVEL_GLO_PHY_L4_MY_008_047/download?dataset=cmems_obs-sl_glo_phy-ssh_my_allsat-l4-duacs-0.25deg_P1D (Global Ocean Gridded L 4 Sea Surface Heights And Derived Variables Reprocessed, 1993 Ongoing). ERA5 reanalysis is available at https://cds.climate.copernicus.eu/datasets/reanalysis-era5-single-levels?tab=overview (Copernicus Climate Change Service Climate Data Store, 2023; Hersbach et al., 2023). The NAO data sets were available at https://psl.noaa.gov/data/timeseries/daily/NAO/ and https://www.cpc.ncep.noaa.gov/products/precip/CWlink/teleconnections/daily/scn/. OSNAP gridded product is available at https://www.o-snap.org/data-access/ (Fu et al., 2023). The moorings IB2, IB3, IB4, and IB5 are available at https://www.o-snap.org/data-access/ and at https://www.bodc.ac.uk/data/published_data_library/catalogue/10.5285/2c01606b-d80a-72a8-e063-7086abc06745/ (Dotto et al., 2025). All figures and analyses were made in Matlab R2023a software (The MathWorks Inc., 2023).

Acknowledgments
The authors would like to thank the captains, crews, and technicians for assisting in the seagoing operations supporting this research. This analysis is a contribution to U.K. Natural Environment Research Council (NERC) National Capability programs CLASS (NE/R015953/1) and AtlantiS (NE/Y005589/1), and NERC grants UK-OSNAP (NE/K010875/1 and NE/K010875/2) and U.K. OSNAP Decade (NE/T00858X/1). WEJ was financed by the U.S. National Science Foundation(OCE-1259398 and OCE-1756231). GEBCO Bathymetric Compilation Group (2023) GEBCO 2023 Grid (https://doi.org/10.5285/f98b053b-0cbc-6c23-e053-6c86abc0af7b).

References

Årthun, M., Eldevik, T., & Smedsrud, L. H. (2019). The role of Atlantic heat transport in future Arctic winter sea ice loss. *Journal of Climate*, *32*(11), 3327–3341. https://doi.org/10.1175/JCLI-D-18-0750.1

Bacon, S. (1997). Circulation and fluxes in the North Atlantic between Greenland and Ireland. *Journal of Physical Oceanography*, *27*, 1420–1435. https://doi.org/10.1175/1520-0485(1997)027<1420:CAFITN>2.0

Berx, B., Hansen, B., Østerhus, S., Larsen, K. M., Sherwin, T., & Jochumsen, K. (2013). Combining in situ measurements and altimetry to estimate volume, heat and salt transport variability through the Faroe–Shetland Channel. *Ocean Science*, *9*(4), 639–654. https://doi.org/10.5194/os-9-639-2013

Biló, T. C., Straneo, F., Holte, J., & Le Bras, I. A.-A. (2022). Arrival of new great salinity anomaly weakens convection in the Irminger Sea. *Geophysical Research Letters*, *49*(11), e2022GL098857. https://doi.org/10.1029/2022GL098857

Chafik, L., Holliday, N. P., Bacon, S., Baker, J. A., Desbruyères, D., Frajka-Williams, E., & Jackson, L. C. (2023). Observed mechanisms activating the recent subpolar North Atlantic warming since 2016. *Philosophical Transactions of the Royal Society A*, *381*(2262), 20220183. https://doi.org/10.1098/rsta.2022.0183

Chafik, L., Rossby, T., & Schrum, C. (2014). On the spatial structure and temporal variability of poleward transport between Scotland and Greenland. *Journal of Geophysical Research: Oceans*, *119*(2), 824–841. https://doi.org/10.1002/2013JC009287

Copernicus Climate Change Service (C3S). (2019). Sea surface temperature daily data from 1981 to present derived from satellite observations. [Dataset]. *Copernicus Climate Change Service (C3S) Climate Data Store (CDS)*, https://doi.org/10.24381/cds.cf608234

Copernicus Climate Change Service, Climate Data Store. (2023). ERA5 hourly data on single levels from 1940 to present. [Dataset]. *Copernicus Climate Change Service (C3S) Climate Data Store (CDS)*, https://doi.org/10.24381/cds.adbb2d47

Desbruyères, D., Chafik, L., & Maze, G. (2021). A shift in the ocean circulation has warmed the subpolar North Atlantic Ocean since 2016. *Communications Earth & Environment*, *2*, 1–9. https://doi.org/10.1038/s43247-021-00120-y

Desbruyères, D. G., Sinha, B., McDonagh, E. L., Josey, S. A., Holliday, N. P., Smeed, D. A., et al. (2020). Importance of boundary processes for heat uptake in the subpolar North Atlantic. *Journal of Geophysical Research: Oceans*, *125*(9), e2020JC016366. https://doi.org/10.1029/2020JC016366

Dotto, T. S., Firing, Y. L., Drysdale, L., & Rayner, D. (2025). *Microcat, current meter and ADCP data from moorings of the Eastern Iceland Basin array as part of UK OSNAP (overturning in the subpolar North Atlantic programme) from 2020-2022*. NERC EDS British Oceanographic Data Centre NOC. https://doi.org/10.5285/2c01606b-d80a-72a8-e063-7086abc06745

Eden, C., & Willebrand, J. (2001). Mechanism of interannual to decadal variability of the North Atlantic circulation. *Journal of Climate*, *14*(10), 2266–2280. https://doi.org/10.1175/1520-0442(2001)014(2266:MOITDV)2.0

Emery, W. J., & Thomson, R. E. (2004). *Data analysis methods in physical oceanography* (2nd ed.). Elsevier.

Evans, D. G., Holliday, N. P., Bacon, S., & Le Bras, I. (2023). Mixing and air–sea buoyancy fluxes set the time-mean overturning circulation in the subpolar North Atlantic and Nordic Seas. *Ocean Science*, *19*(3), 745–768. https://doi.org/10.5194/os-19-745-2023

Foukal, N. P., & Lozier, M. S. (2017). Assessing variability in the size and strength of the North Atlantic subpolar gyre. *Journal of Geophysical Research: Oceans*, *122*(8), 6295–6308. https://doi.org/10.1002/2017JC012798

Foukal, N. P., & Lozier, M. S. (2018). Examining the origins of ocean heat content variability in the eastern North Atlantic subpolar gyre. *Geophysical Research Letters*, *45*(20), 11275–11283. https://doi.org/10.1029/2018GL079122

Fraser, N. J., Cunningham, S. A., Drysdale, L. A., Inall, M. E., Johnson, C., Jones, S. C., et al. (2022). North Atlantic current and European slope current circulation in the Rockall Trough observed using moorings and gliders. *Journal of Geophysical Research: Oceans*, *127*(12), e2022JC019291. https://doi.org/10.1029/2022JC019291

Fu, Y., Lozier, M. S., Biló, T. C., Bower, A. S., Cunningham, S. A., Cyr, F., et al. (2023). Seasonality of the meridional overturning circulation in the subpolar North Atlantic. *Communications Earth & Environment*, *4*(1), 181. https://doi.org/10.1038/s43247-023-00848-9

Gary, S. F., Cunningham, S. A., Johnson, C., Houpert, L., Holliday, N. P., Behrens, E., et al. (2018). Seasonal cycles of oceanic transports in the eastern subpolar North Atlantic. *Journal of Geophysical Research: Oceans*, *123*(2), 1471–1484. https://doi.org/10.1002/2017JC013350

GEBCO Bathymetric Compilation Group. (2023). *The GEBCO_2023 Grid–A continuous terrain model of the global oceans and land*. NERC EDS British Oceanographic Data Centre NOC. https://doi.org/10.5285/f98b053b-0cbc-6c23-e053-6c86abc0af7b

Global Ocean Gridded L 4 Sea Surface Heights And Derived Variables Reprocessed. (1993). Ongoing. E.U. Copernicus marine Service information (CMEMS) [Dataset]. *Marine Data Store (MDS)*. https://doi.org/10.48670/moi-00148

Good, S., Fiedler, E., Mao, C., Martin, M. J., Maycock, A., Reid, R., et al. (2020). The current configuration of the OSTIA system for operational production of foundation sea surface temperature and ice concentration analyses. *Remote Sensing*, *12*(4), 720. https://doi.org/10.3390/rs12040720

Grinsted, A., Moore, J. C., & Jevrejeva, S. (2004). Application of the cross wavelet transform and wavelet coherence to geophysical time series. *Nonlinear Processes in Geophysics*, *11*(5/6), 561–566. https://doi.org/10.5194/npg-11-561-2004

Häkkinen, S., & Rhines, P. (2004). Decline of subpolar North Atlantic circulation during the 1990s. *Science*, *304*(5670), 555–559. https://doi.org/10.1126/science.1094917

Häkkinen, S., Rhines, P. B., & Worthen, D. L. (2011a). Warm and saline events embedded in the meridional circulation of the northern North Atlantic. *Journal of Geophysical Research*, *116*(C3), C03006. https://doi.org/10.1029/2010JC006275

Häkkinen, S., Rhines, P. B., & Worthen, D. L. (2011b). Warm and saline events embedded in the meridional circulation of the northern North Atlantic. *Journal of Geophysical Research*, *116*, C03006. https://doi.org/10.1029/2010JC006275

Hansen, B., Larsen, K. M. H., Hátún, H., Olsen, S. M., Gierisch, A. M. U., Østerhus, S., & Ólafsdóttir, S. R. (2023). The Iceland–Faroe warm-water flow towards the Arctic estimated from satellite altimetry and in situ observations. *Ocean Science*, *19*(4), 1225–1252. https://doi.org/10.5194/os-19-1225-2023

Hátún, H., Sandø, A. B., Drange, H., Hansen, B., & Valdimarsson, H. (2005). Influence of the Atlantic subpolar gyre on the thermohaline circulation. *Science*, *309*(5742), 1841–1844. https://doi.org/10.1126/science.1114777

Hersbach, H., Bell, B., Berrisford, P., Biavati, G., Horányi, A., Muñoz Sabater, J., et al. (2023). ERA5 hourly data on single levels from 1940 to present. [Dataset]. *Copernicus Climate Change Service (C3S) Climate Data Store (CDS)*, https://doi.org/10.24381/cds.adbb2d47

Hersbach, H., Bell, B., Berrisford, P., Hirahara, S., Horányi, A., Muñoz-Sabater, J., et al. (2020). The ERA5 global reanalysis. *Quarterly Journal of the Royal Meteorological Society*, *146*(730), 1999–2049. https://doi.org/10.1002/qj.3803

Heywood, K. J., McDonagh, E. L., & White, M. A. (1994). Eddy kinetic energy of the North Atlantic subpolar gyre from satellite altimetry. *Journal of Geophysical Research*, *99*(C11), 22525–22539. https://doi.org/10.1029/94JC01740

Holliday, N. P., Bersch, M., Berx, B., Chafik, L., Cunningham, S., Florindo-López, C., et al. (2020). Ocean circulation causes the largest freshening event for 120 years in eastern subpolar North Atlantic. *Nature Communications*, *11*(1), 585. https://doi.org/10.1038/s41467-020-14474-y

Houpert, L., Cunningham, S., Fraser, N., Johnson, C., Holliday, N. P., Jones, S., et al. (2020). Observed variability of the North Atlantic current in the Rockall trough from 4 years of mooring measurements. *Journal of Geophysical Research: Oceans*, *125*(10), e2020JC016403. https://doi.org/10.1029/2020JC016403

Houpert, L., Inall, M. E., Dumont, E., Gary, S., Johnson, C., Porter, M., et al. (2018). Structure and transport of the North Atlantic current in the eastern subpolar gyre from sustained glider observations. *Journal of Geophysical Research: Oceans*, *123*(8), 6019–6038. https://doi.org/10.1029/2018JC014162

Khatri, H., Williams, R. G., Woollings, T., & Smith, D. M. (2022). Fast and slow subpolar ocean responses to the North Atlantic oscillation: Thermal and dynamical changes. *Geophysical Research Letters*, *49*(24), e2022GL101480. https://doi.org/10.1029/2022GL101480

Koman, G., Johns, W. E., Houk, A., Houpert, L., & Li, F. (2022). Circulation and overturning in the eastern North Atlantic subpolar gyre. *Progress in Oceanography*, *208*, 102884. https://doi.org/10.1016/j.pocean.2022.102884

Kondetharayil Soman, A., Chafik, L., & Nilsson, J. (2022). Linking coherent anticyclonic eddies in the Iceland Basin to decadal oceanic variability in the subpolar North Atlantic. *Journal of Geophysical Research: Oceans*, *127*(5), e2021JC018046. https://doi.org/10.1029/2021JC018046

Koul, V., Tesdal, J.-E., Bersch, M., Hátún, H., Brune, S., Borchert, L., et al. (2020). Unraveling the choice of the North Atlantic subpolar gyre index. *Scientific Reports*, *10*(1), 1005. https://doi.org/10.1038/s41598-020-57790-5

Li, F., Lozier, M. S., Bacon, S., Bower, A. S., Cunningham, S. A., de Jong, M. F., et al. (2021). Subpolar North Atlantic western boundary density anomalies and the meridional overturning circulation. *Nature Communications*, *12*(1), 3002. https://doi.org/10.1038/s41467-021-23350-2

Lohmann, K., Drange, H., & Bentsen, M. (2009). Response of the North Atlantic subpolar gyre to persistent North Atlantic oscillation like forcing. *Climate Dynamics*, *32*(2–3), 273–285. https://doi.org/10.1007/s00382-008-0467-6

Lozier, M. S., Li, F., Bacon, S., Bahr, F., Bower, A. S., Cunningham, S. A., et al. (2019). A sea change in our view of overturning in the subpolar North Atlantic. *Science*, *363*(6426), 516–521. https://doi.org/10.1126/science.aau6592

Marsh, R., Haigh, I. D., Cunningham, S. A., Inall, M. E., Porter, M., & Moat, B. I. (2017). Large-scale forcing of the European slope current and associated inflows to the North sea. *Ocean Science*, *13*(2), 315–335. https://doi.org/10.5194/os-13-315-2017

Marshall, J., Johnson, H., & Goodman, J. (2001). A study of the interaction of the North Atlantic oscillation with ocean circulation. *Journal of Climate*, *14*(7), 1399–1421. https://doi.org/10.1175/1520-0442(2001)014⟨1399:ASOTIO⟩2.0

McCarthy, G. D., Smeed, D. A., Johns, W. E., Frajka-Williams, E., Moat, B. I., Rayner, D., et al. (2015). Measuring the Atlantic meridional overturning circulation at 26°N. *Progress in Oceanography*, *130*, 91–111. https://doi.org/10.1016/J.POCEAN.2014.10.006

McDougall, T. J., & Barker, P. M. (2011). Getting started with TEOS-10 and the Gibbs Seawater (GSW) oceanographic toolbox. *SCOR/IAPSO WG*, *127*, 1–28.

Megann, A., Blaker, A., Josey, S., New, A., & Sinha, B. (2021). Mechanisms for late 20th and early 21st century decadal AMOC variability. *Journal of Geophysical Research: Oceans*, *126*(12), e2021JC017865. https://doi.org/10.1029/2021JC017865

Mercier, H., Desbruyères, D., Lherminier, P., Velo, A., Carracedo, L., Fontela, M., & Pérez, F. F. (2024). New insights into the eastern subpolar North Atlantic meridional overturning circulation from OVIDE. *Ocean Science*, *20*(3), 779–797. https://doi.org/10.5194/os-20-779-2024

Mercier, H., Lherminier, P., Sarafanov, A., Gaillard, F., Daniault, N., Desbruyères, D., et al. (2015). Variability of the meridional overturning circulation at the Greenland-Portugal OVIDE section from 1993 to 2010. *Progress in Oceanography*, *132*, 250–261. https://doi.org/10.1016/J.POCEAN.2013.11.001

Petit, T., Lozier, M. S., Josey, S. A., & Cunningham, S. A. (2020). Atlantic deep water formation occurs primarily in the Iceland Basin and Irminger Sea by local buoyancy forcing. *Geophysical Research Letters*, *47*(22), e2020GL091028. https://doi.org/10.1029/2020GL091028

Pollard, R. T., Read, J. F., Holliday, N. P., & Leach, H. (2004). Water masses and circulation pathways through the Iceland Basin during Vivaldi 1996. *Journal of Geophysical Research*, *109*(C4), C04004. https://doi.org/10.1029/2003JC002067

Roemmich, D., & Gilson, J. (2009). The 2004–2008 mean and annual cycle of temperature, salinity, and steric height in the global ocean from the Argo Program. *Progress in Oceanography*, *82*(2), 81–100. https://doi.org/10.1016/J.POCEAN.2009.03.004

Roessler, A., Rhein, M., Kieke, D., & Mertens, C. (2015). Long-term observations of North Atlantic current transport at the gateway between Western and Eastern Atlantic: NAC transport observations at MAR. *Journal of Geophysical Research: Oceans*, *120*(6), 4003–4027. https://doi.org/10.1002/2014JC010662

Roussenov, V. M., Williams, R. G., Lozier, M. S., Holliday, N. P., & Smith, D. M. (2022). Historical reconstruction of subpolar North Atlantic overturning and its relationship to density. *Journal of Geophysical Research: Oceans*, *127*(6), e2021JC017732. https://doi.org/10.1029/2021JC017732

Sarafanov, A., Falina, A., Mercier, H., Sokov, A., Lherminier, P., Gourcuff, C., et al. (2012). Mean full-depth summer circulation and transports at the northern periphery of the Atlantic ocean in the 2000s. *Journal of Geophysical Research*, *117*(C1), C01014. https://doi.org/10.1029/2011JC007572

Shoosmith, D. R., Richardson, P. L., Bower, A. S., & Rossby, H. T. (2005). Discrete eddies in the northern North Atlantic as observed by looping RAFOS floats. *Deep Sea Research Part II*, *52*(3–4), 627–650. https://doi.org/10.1016/J.DSR2.200

The MathWorks Inc. (2023). MATLAB version: 9.14.0 (R2023a). *The MathWorks Inc*, Retrieved from https://www.mathworks.com

van Aken, H. M., & Becker, G. (1996). Hydrography and through-flow in the north-eastern North Atlantic Ocean: The NANSEN project. *Progress in Oceanography*, *38*(4), 297–346. https://doi.org/10.1016/S0079-6611(97)00005-0

Zhao, J., Bower, A., Yang, J., Lin, X., & Holliday, N. P. (2018). Meridional heat transport variability induced by mesoscale processes in the subpolar North Atlantic. *Nature Communications*, *9*(1), 1124. https://doi.org/10.1038/s41467-018093134-x

Zhao, J., Bower, A., Yang, J., Lin, X., & Zhou, C. (2018). Structure and formation of anticyclonic eddies in the Iceland Basin. *Journal of Geophysical Research: Oceans*, *123*(8), 5341–5359. https://doi.org/10.1029/2018JC013886